Synchrotron X-ray reciprocal-space mapping, topography and diffraction resolution studies of macromolecular crystal quality

T. J. Boggon,[a]† **J. R. Helliwell,**[a] **R. A. Judge,**[b] **A. Olczak,**[a] **D. P. Siddons,**[c]* **E. H. Snell**[b] **and V. Stojanoff**[d]

[a]Chemistry Department, University of Manchester, Oxford Road, Manchester M13 9PL, England, [b]NASA Laboratory for Structural Biology, Code SD48, MSFC, Huntsville, AL 35812, USA, [c]NSLS, Brookhaven National Laboratory, Upton, New York 11973, USA, and [d]ESRF, BP220, Grenoble CEDEX, France

† Current address: Mount Sinai School of Medicine, 1425 Madison Avenue, Box 1667, New York, NY 10029-6574, USA.

Correspondence e-mail: siddons@bnl.gov

A comprehensive study of microgravity and ground-grown chicken egg-white lysozyme crystals is presented using synchrotron X-ray reciprocal-space mapping, topography techniques and diffraction resolution. Microgravity crystals displayed reduced intrinsic mosaicities on average, but no differences in terms of strain over their ground-grown counterparts. Topographic analysis revealed that in the microgravity case the majority of the crystal was contributing to the peak of the reflection at the appropriate Bragg angle. In the ground-control case only a small volume of the crystal contributed to the intensity at the diffraction peak. The techniques prove to be highly complementary, with the reciprocal-space mapping providing a quantitative measure of the crystal mosaicity and strain (or variation in lattice spacing) and the topography providing a qualitative overall assessment of the crystal in terms of its X-ray diffraction properties. Structural data collection was also carried out at the synchrotron.

1. Introduction

Macromolecular structural crystallography requires the growth of high-quality crystals, where quality is defined as being strongly diffracting and radiation-insensitive. During the crystal-growth process macromolecules diffuse to the crystal surface and are incorporated into the crystal lattice. When incorporation kinetics are faster than diffusive transport, a solute-concentration gradient forms around the growing crystal, with the solute concentration close to the crystal surface being less than that of the bulk solution. On earth, this 'depletion zone' (McPherson et al., 1999) leads to buoyancy-driven convection as the less dense solute-reduced solution rises (Baird et al., 1986; Fehribach & Rosenberger, 1989; Grant & Saville, 1991; Lin et al., 1995). Buoyancy-driven convection observed in studies of protein crystal growth (Pusey et al., 1986, 1988) accelerates solute transport to crystal faces, increasing the growth rate and allowing spatial irregularities and temporal oscillations in solute transport to occur so that defective regions in the crystal can form (Nerad & Shlichta, 1986; Monaco & Rosenberger, 1993; Vekilov & Rosenberger, 1996). Reduction of the depletion-zone volume lessens the benefits of lower supersaturation around the crystal. In a large depletion zone, more time is available for a growth unit arriving at a growing crystal face to orientate and adapt to a minimum-energy attachment on the crystal face before becoming restricted by subsequent neighbor molecules. Over-celerity of crystal growth can result in molecules being trapped in high-energy configurations inconsistent with the regular

periodic crystal lattice, and long-range disorders can arise including those described by the mosaic block theory (Darwin, 1922; Nerad & Shlichta, 1986; Helliwell, 1988; Teeter *et al.*, 1993; Fourme *et al.*, 1995). These can deleteriously affect the weak high-resolution data for the crystal (Helliwell, 1988). Sedimentation, another gravity-driven effect, can also have a negative effect on crystal growth as crystals fall through solution to the bottom of the growth chamber and also by either large or insoluble impurities or aggregates sedimenting onto the face of growing crystals. Incorporation of such impurities causes decreases in long-range crystal order (Lang, 1957; Binnig *et al.*, 1986; Kuznetsov *et al.*, 1996) and crystal sedimentation interferes with crystal morphology and nucleation itself. The effects of buoyant convection and sedimentation (Wilcox, 1983) are therefore thought to be damaging to crystal perfection and X-ray diffraction quality.

Growth in microgravity is seen as a means of overcoming convective flow, although it shifts its range not its occurance (Pusey *et al.*, 1986, 1988). It also reduces sedimentation effects, providing opportunities for growing higher quality crystals through the establishment of stable depletion zones. To date results from microgravity have been mixed, with enhancements in some studies (McPherson, 1993; Delucas *et al.*, 1994; Ng *et al.*, 1997) and no positive or even detrimental effects in others (Hilgenfeld *et al.*, 1992). In part, this has been a consequence of the variation of experimental techniques for crystal growth (*e.g.* vapor diffusion, batch or dialysis methods) and X-ray analysis (*e.g.* X-ray source, definition of resolution, data-collection method, detectors and processing protocol). Diagnostic experiments on the growth process itself have also revealed some surprises in microgravity crystal growth, *e.g.* the presence of Marangoni convection (Marangoni, 1871; Savino & Monti, 1996; Molenkamp, 1998) in vapor-diffusion geometry (Chayen *et al.*, 1997) and the effect of *g*-jitter on the process (Long *et al.*, 1994; Snell, Boggon *et al.*, 1997). Additionally, the hardware available for microgravity experiments is functionally limited. We were fortunate to be able to fly in the European Space Agency's (ESA) Advanced Protein Crystallization Facility (APCF; Snyder *et al.*, 1991; Bosch *et al.*, 1992) with temperature control to ±0.1 K. Many microgravity experiments make use of the Single-Locker Thermal Enclosure System (STES), which has a single temperature-controlled wall. Samples close to the wall experience temperature control (at ambient temperatures) of ±0.5 K, whilst those further away may experience temperature differences as large as ±1.5 K. At non-ambient temperatures the variation is worse. These experimental limitations [variable *g*-level depending on the mission and astronaut activity, Marangoni motions for phase-boundary systems and temperature control (excepting the APCF) worse than the home laboratory] make current scientific use difficult. Future hardware intended for the International Space Station will hopefully overcome these difficulties.

The use of mosaicity studies (*e.g.* Snell, 1998) and topography (Stojanoff & Siddons, 1996) was introduced as an approach which removed the variations in the X-ray techniques used to study crystal samples. The measurement of X-ray mosaicity was pioneered (Helliwell, 1988; Colapietro *et al.*, 1992) as a direct indicator of the physical perfection of the macromolecular crystal. The mosaicity provides a simple measurement of crystal quality independent of many experimental parameters. It has been used to characterize successfully the improvement seen in some microgravity samples *i.e.* a reduction in the reflection mosaic spread providing a corresponding increase in the signal-to-noise ratio of the reflection (Snell *et al.*, 1995; Helliwell *et al.*, 1996; Ng *et al.*, 1997). Mosaicity is the recorded rocking width of the reflection with the instrument contribution deconvoluted. As such, it requires a beam with geometric and spectral divergence that do not mask the measurements being made (Greenhough & Helliwell, 1982). The mosaicity measured from the crystal is a global measure of several effects. Simple rocking-curve measurements cannot separate out the effects arising from strains (*i.e.* *d*-spacing variations) from those arising from classical mosaicity, which involves only rotational misalignments of parts of the crystal. This separation requires that 2θ be determined precisely as well as θ (also termed ω). The technique used for this purpose is the triple-axis spectrometer (Brockhouse, 1955), first used for neutron-scattering studies. It will be described in detail later.

If we wish to reach a microscopic understanding of the crystal defects so that their origin may be identified, diffraction imaging (*i.e.* X-ray diffraction topography) can be a useful tool. It allows the diffracting power of a crystal to be spatially resolved on the micrometer level at an arbitrary sample orientation. Thus, a precise picture of which parts of the sample diffract at which incidence angles can be built up. If the defect density is low enough, it should be possible to determine the nature of an individual defect. X-ray topography has been carried out on lysozyme (Stojanoff & Siddons, 1996; Stojanoff *et al.*, 1996, 1997; Dobrianov *et al.*, 1998; Otalora *et al.*, 1999; Fourme *et al.*, 1999) and other proteins such as apocrustacyanin and insulin by the present authors.

Mosaicity analysis in combination with X-ray topography was first suggested by Shaikevitch & Kam (1981). Here, we present the combination of reciprocal-space mapping techniques, topography and conventional structural data collection, allowing the sample to be completely characterized and illustrating the complementary nature of the techniques.

2. Theoretical considerations

2.1. Long-range and short-range order

Disorder in a periodic structure can be characterized by a correlation length, *i.e.* a length over which it is possible to predict the location of the next repeat unit based on the lattice parameters. It is thus common to talk about the limiting cases of this parameter, *i.e.* long-range and short-range disorder. In general, long-range phenomena in real space give rise to localized effects in reciprocal space and *vice versa*. We might thus expect that long-range disorder will change the distribution of scattering power in the immediate vicinity of reciprocal-lattice points, whereas short-range disorder will

contribute scattering power more or less uniformly throughout reciprocal space, *i.e.* diffuse scatter. Thermal disorder is a particular example of the latter.

Crystal mosaic theory (Darwin, 1922) proposes an approximation to the continuous distribution of disorders observed in nature. In this model, the crystal is composed of
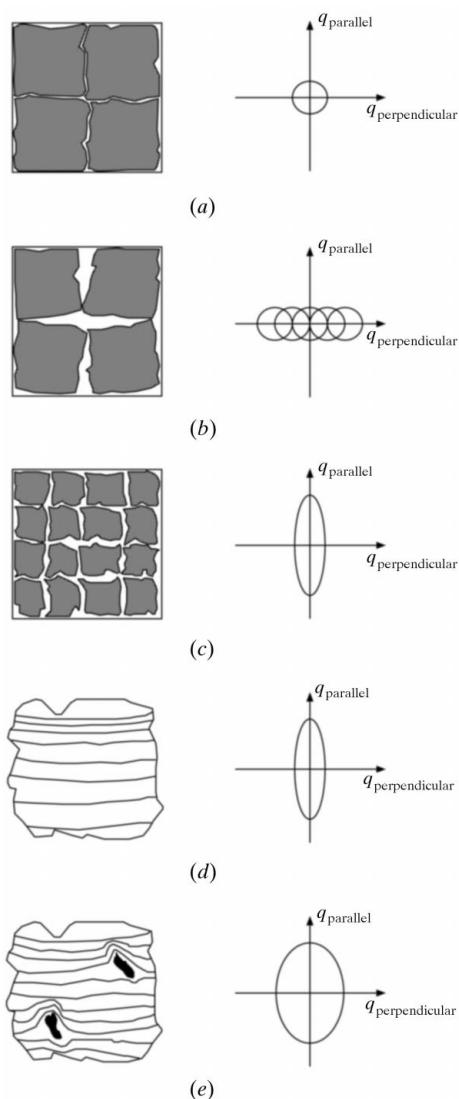

Figure 1
Schematic diagram illustrating the influence of various crystal defects on the reciprocal-space map. In (*a*) the crystal has mosaic structure, but all the blocks are well aligned so that their contributions to the reciprocal space map (RSM) overlap. In (*b*), there is significant misalignment of the blocks, so their RSM peaks are distributed along $q_{\text{perpendicular}}$. Note that this causes no broadening along q_{parallel}. In (*c*), the blocks are again well aligned, but there are many of them and they are small. Thus, there is a finite size influence on the RSM, which broadens it along q_{parallel}. In (*d*), the grains are well aligned and are large (only one is shown in the diagram), but the *d* spacing varies throughout the block. This also causes a broadening along q_{parallel}. Cases (*c*) and (*d*) can only be distinguished by making measurements at different diffraction orders. The size effect is independent of order, whereas the strain effect increases with increasing diffraction order. (*e*) represents a more realistic view of a real crystal, in which point, line and plane defects all mix continuously to create effectively a domain structure. In this case, the RSM is smeared in both dimensions.

microscopic regions of perfectly ordered material assembled into a macroscopic object in such a way that there are small misorientations between the perfect regions. The boundaries between such regions are ignored and no model for them is proposed. The assumption is also made that the number of such blocks is large in a given sample. The model is useful in that reasonably accurate calculations of diffracted intensities can be made from it under certain conditions. It does not describe accurately the defect structure and morphology of real crystals.

The opposite viewpoint starts from a perfect crystal block and introduces well defined defects such as vacancies, dislocations and stacking faults and attempts to calculate the diffracted intensities from first principles. This has led to the development of the dynamical theory of diffraction in distorted crystals (*e.g.* Taupin, 1964; Takagi, 1969; Kato, 1980). The application of this theory to the calculation of the microscopic intensity variations within a diffraction spot is quite well developed for relatively simple defect configurations. For crystals such as the ones we discuss in this work, such methods are, in general, inapplicable owing to the relatively high defect densities observed. In the following, we will discuss our results in terms of the mosaic model.

Bragg & Nye (1947) give an excellent pictorial representation of the mosaic model. Long-range disorder can be manifest in three major ways (Nave, 1998). Fig. 1(*a*) shows a crystal with mosaic blocks all well aligned. The reciprocal-space representation of this is essentially that of a perfect crystal (Fig. 1*a*). The most obvious disorder in an array of mosaic blocks such as that in Fig. 1(*a*) is an angular misalignment of the blocks. In reciprocal space, this causes the reciprocal-lattice point (RLP) to be smeared out in a direction perpendicular to the reciprocal-lattice vector (RLV). We will refer to this direction as $q_{\text{perpendicular}}$. This is illustrated in Fig. 1(*b*). Note that there is no change in the map parallel to the RLV (q_{parallel}).
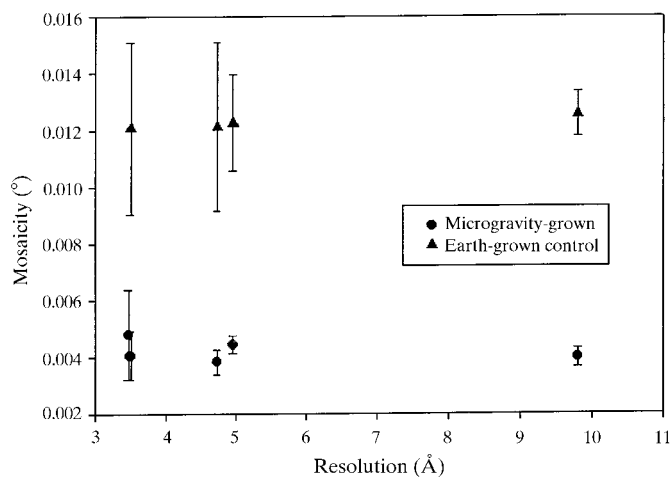

Figure 2
Plot of mosaicity *versus* resolution for data collected from microgravity and ground-control lysozyme crystals (Snell *et al.*, 1995; Helliwell *et al.*, 1996). A minimum of four reflections were used for each point plotted. The mosaicity values are resolution-independent based on these data.

If the mosaic blocks are very small, then the finite size gives rise to a smearing of the RLP in the direction parallel to the RLV, as illustrated in Fig. 1(c). Again, note that this has no effect on $q_{\text{perpendicular}}$, i.e. these two effects are orthogonal.

Another mechanism for producing smearing in the q_{parallel} direction is lattice strain. If the lattice parameter is a function of position in the crystal, as may be caused by inhomogeneous elastic deformations of the crystal, then the X-ray beam samples all of them and the reciprocal-space map (RSM) is elongated along the RLV (Fig. 1d).

The presence of inclusions or lattice defects such as dislocations can cause combinations of dilations and rotations of the lattice, as illustrated in Fig. 1(e). This will produce smearing in both $q_{\text{perpendicular}}$ and q_{parallel}.

The situation in real crystals is much more akin to the situation of Fig. 1(e) than the others. If one considers the mosaic block size as the correlation length in the crystal, then the results are similar. However, the traditional mosaic model does not take account of lattice strains.

In a rocking-curve study by Snell (1998), an attempt to separate strain and domain misalignment was made. Mosaicity (rocking-curve width with spectral and geometric parameters deconvoluted) was plotted against resolution for a microgravity and ground-control crystal of chicken egg-white lysozyme from the IML-2 mission (Fig. 2). Sampling took place using a minimum of four reflections for each resolution point plotted. If strains were significant then the 'mosaicity' should increase as a function of diffraction order. Little or no resolution contribution in the microgravity case was seen; hence, the dominant effects on mosaicity were internal domain volumes and their misalignment. A similar observation cannot be ruled out for the ground controls because of the size of the 'error bars' (spread of volumes, each of which is measured with a certain error of $\sim 0.002°$).

In order to separate the different effects, we used a triple-axis diffractometer to evaluate the reciprocal-space map (Fewster, 1997). This allows the variation in d spacing (Fig. 1d) to be deconvoluted from that of volume and misalignment (Figs. 1b and 1c). With the use of X-ray topography, we can additionally visualize the long-range misalignment properties. These two methods are discussed in the following sections.
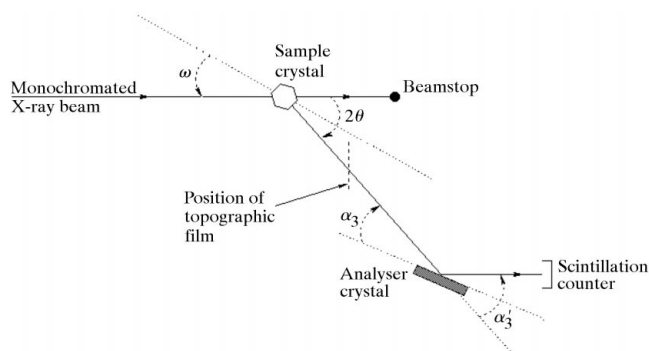
2.2. Triple-axis diffractometry and reciprocal-space mapping

Rocking-width studies analyze the angular range of a reflection. A two-axis instrument is normally used: one axis for the sample and the other for the monochromator. The rocking width recorded is a convolution of the sample and instrument parameters, i.e. geometric and spectral divergence (Greenhough & Helliwell, 1982). The instrument parameters are routinely deconvoluted (e.g. Colapietro et al., 1992) to give a sample mosaicity value which can be compared directly between different experiments. However, for these mosaicity studies there is effectively an integration of measured intensity over a relatively wide range of reciprocal space at the crystal rotation angles under investigation. Information contained in the shape of the reciprocal-lattice point, such as the size of the diffracting volume (e.g. defects that disrupt the atomic plane and distance between defects or distortions), is therefore lost. This information can be quantified by using the technique of reciprocal-space mapping.

Reciprocal-space mapping differs from the technique of rocking-width (or mosaicity) measurement by incorporation of a third 'analyzer' crystal. The setup is termed a triple-axis diffractometer and consists of the monochromator, the sample and the analyzer crystal (Fig. 3). This allows reciprocal space to be surveyed in two dimensions (Fig. 4).

The first crystal (the monochromator) selects the wavelength from the polychromatic incident synchrotron radiation and collimates the beam to the intrinsic width of the monochromator reflection [in this case Si(111)]. The beam from the monochromator is incident on the sample. The analyzer crystal (made of the same material as the monochromator) gives a very fine probe of reciprocal space compared with
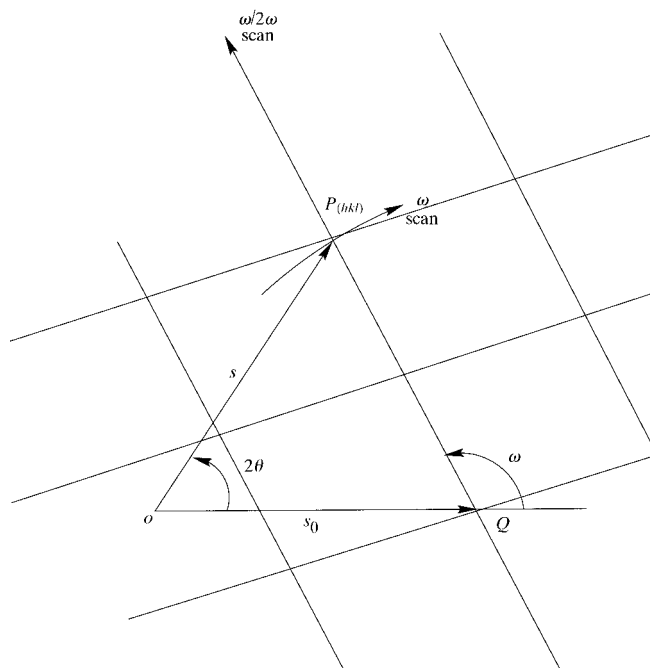

Figure 3
Schematic arrangement of the triple-axis diffractometer setup. To record the reciprocal-space map the axes ω and 2θ are scanned (the first axis being that of the monochromator).

Figure 4
Reciprocal-space diagram illustrating ω and $\omega/2\theta$ scanning techniques. Adapted from Alexander & Smith (1962).

rocking-width studies. Fig. 5 illustrates the area integrated by the double-axis (rocking width) and triple-axis (reciprocal-space mapping) techniques. The contribution of the instrument on the measurements can be seen from the way wavelength dispersion, geometric divergence and detector acceptance affect the integrating area of the reciprocal-space probe. Obviously, the smaller the probe the greater the detail in which reciprocal space can be scanned.

The signal recorded at the detector is a convolution of the signal from the sample and the instrument function. The instrument function is calculated according to Holý & Mikulík (1996). This can be deconvoluted from the measurements and the diffraction-space map converted to reciprocal space by a simple geometric relationship (Fewster & Andrew, 1993; Holý & Mikulík, 1996; Fewster, 1996). Reciprocal space is expressed in terms of $q_{parallel}$ and $q_{perpendicular}$ vectors parallel and perpendicular to the scattering vector, $\mathbf{S}$, respectively. Domain-misalignment effects are seen in the $q_{perpendicular}$ direction (Fig. 1b), whilst variation in d^* spacing and volume effects are seen in the $q_{parallel}$ direction (Figs. 1c and 1d). This reciprocal space has dimensions of $2\pi/\lambda$ (rather than $1/\lambda$).

2.3. X-ray topography

The X-ray topographic method is based on reflection of X-rays by a set of lattice planes, where irregularities in the crystal lattice cause locally changing diffracted intensities (contrast) in topographic images of individual reflections. Topographs are then a measure of the scattering power of the crystal as a function of position across the diffracted X-ray beam (Tanner, 1996). Essentially, it is an image of the diffracting parts of the crystal at a particular orientation. In most cases, it is not the defect itself but the lattice deformations surrounding the defect which produce the X-ray topographic contrast. Intensity variations are related to the type and volume distribution of defects. Unfocused highly parallel monochromatic X-rays, as used in this study, give rise to three types of contrast in the images. Orientation contrast occurs where effective misorientation by mosaic domain rotation or

lattice dilations exceeds the residual divergence of the X-ray beam. Zero intensity corresponds geometrically to the misorientated region. Extinction contrast arises where the crystal strain gradient is high, such as around a dislocation or impurity inclusion. The scattering power around the defect differs from that in the rest of the crystal. Dynamical contrast originates from dynamical theory and is unlikely for weakly scattering macromolecular crystals, although it may have been observed in some studies (Otalora et al., 1999). A high-quality region of the crystal will have a uniform dark or light area on the topograph.

The maximum spatial resolution obtainable in an X-ray topograph is about 2–3 µm with photographic film and 1 µm with nuclear emulsion plates. Its resolution is not as high as other crystal-quality visualization methods [i.e. atomic force microscopy (AFM) and electron microscopy (EM)], but it is not as destructive, requires no sample preparation and crystals can be used for further analysis immediately before or afterwards. X-ray topography works best when the defect density is low, complementary to rocking-curve studies which work best for crystals with high defect densities. The methods of topography and reciprocal-space mapping are therefore excellent complements to one another. The introduction and development of X-ray topography for protein crystal perfection studies is described by Fourme et al. (1995), Stojanoff & Siddons (1996), Stojanoff et al. (1996, 1997), Dobrianov et al. (1998) and Otalora et al. (1999).

3. Experimental

3.1. Macromolecular crystal growth

We have used the chicken egg-white protein lysozyme as the test material for our studies. Lysozyme has been well characterized in both ground-based and microgravity-based research by a variety of experimental and theoretical analyses. Although lysozyme's ease of crystallization over a wide range of conditions is not typical for a protein, it is readily available commercially and has long been the standard for research into protein crystal growth.

Commercial lysozyme supplied by Sigma (Lot 111H7010 for the IML-2 mission and Lot 53H7145 for the LMS mission) was used for crystallization without further purification. The dialysis crystallization technique was used, with 15.8 mg of protein dissolved in 188 µl of 0.04 M acetate buffer (pH 4.7) and 1.26 M NaCl and 1.35 M NaCl used as precipitants in the IML-2 and LMS missions, respectively. Crystallization took place in the European Space Agency (ESA) Advanced Protein Crystallization Facility (APCF; Snyder et al., 1991; Bosch et al., 1992) on board the NASA Space Shuttle International Microgravity Laboratory 2 mission (IML-2), STS-65, and on the Life and Microgravity Sciences mission LMS, STS-78. The APCF microgravity crystallization times for the IML-2 mission, carried out in 1994, and the LMS mission, carried out in 1996, were 300 and 370 h, respectively.

Microgravity and ground controls were identically prepared in identical growth reactors. The microgravity
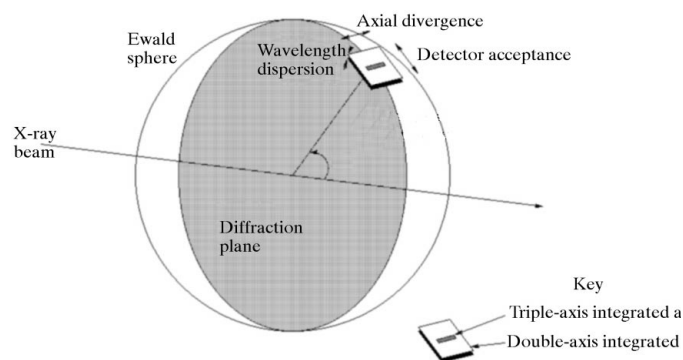

Figure 5
Ewald construction illustrating the area integrated by reciprocal-space mapping of a diffraction spot compared with conventional double-axis mosaicity scanning geometry. Adapted from Fewster (1996).

samples were kept at 293 ± 0.1 K for both missions. For the IML-2 mission, the ground controls were kept in a Styrofoam container providing a stability of ±1 K. For the LMS mission, the ground control was fully thermostatically controlled to the same conditions as the microgravity samples. Mach–Zehnder interferometer (Snell *et al.*, 1996) and CCD video monitoring also took place during the LMS (Boggon *et al.*, 1998) mission; only CCD video monitoring took place during the IML-2 mission (Snell *et al.*, 1997). The crystals were kept in their growth reactors until data collection at National Synchrotron Light Source (NSLS) at the Brookhaven National Laboratory.

3.2. X-ray analyses

RSM data collection for both missions was carried out on the X26C beamline of the NSLS. The source-to-instrument distance was 20 m, with a channel-cut two-reflection Si(111) monochromator providing an intrinsic wavelength bandpass, $\delta\lambda/\lambda$, of 1.3×10^{-4}. The angular extent of the source referred to the sample was of the order of 6×60 μrad^2 ($1'' \times 10''$). The instrument resolution function (IRF'; Colapietro *et al.*, 1992) was calculated to be 0.002° excluding the reflection-dependent $(\Delta\lambda/\lambda)\tan\theta$ component. Several slits were employed to reduce the beam size to 1 mm^2 at the monochromator and sample positions.

The typical experimental protocol for each sample involved initial visual inspection and microphotography of the mounted crystal (for volume and orientation information) followed by recording of a single image-plate oscillation (1 or 2°) X-ray exposure. For both missions, reflections were chosen to be in the plane defined by the incident X-ray beam and a line perpendicular to the spindle axis (equatorial plane). The selected reflections were in the 3–4 Å resolution shell in order to minimize resolution-degrading dispersion effects. X-ray diffraction topographic images were then recorded on Kodak Industrex SR5 film. The film was developed for 6 min in 1:1 Kodak D19 developer and was fixed for 5 min in a Kodak fixer.

For the crystals grown during the first mission (IML-2), only X-ray diffraction topographic images were recorded, since at that time a triple-axis diffractometer was not available. A rather simple experimental setup with a single horizontal axis diffractometer was employed. The wavelength was chosen to be 1.0 Å, a wavelength frequently used in structure-determination data collection. The crystal-to-film distance was set to 100 mm and the exposure time (of the order of 2000 s) was kept constant for all samples. Four ground-control and six microgravity-grown crystals were mounted out of their growth reactor into quartz capillaries with the help of an artificial mother liquor prepared for this purpose.

For the LMS mission a triple-axis diffractometer was used. A channel-cut two-reflection analyzer crystal [similar to the Si(111) monochromator] was used for the reciprocal-space mapping. Measurements were taken using a wavelength of 1.608 Å (calibrated with a cobalt foil). As mentioned above, reflections were selected to have a similar *d* spacing to that of

the monochromator/analyzer, *i.e.* 3–4 Å. The diffractometer used had an angular step size of 0.00025° for both the sample (ω) and analyzer (2θ) axes. A scintillation counter was used as detector when measuring rocking curves and reciprocal-space maps.

Before reciprocal-space mapping measurements were made on the lysozyme crystals, a silicon sample was used to characterize the beam with the analyzer crystal in place. The reciprocal-space profile from a perfect silicon crystal is well known, allowing the instrument effects to be empirically determined. A full theoretical treatment of the instrument effects was also carried out according to Holý & Mikulík (1996). The q_{parallel} and $q_{\text{perpendicular}}$ values for the instrument contribution were 1×10^{-4} and 5×10^{-5}, respectively.

Three ground-control and five microgravity lysozyme crystals grown during the second mission (LMS) were used for the reciprocal-space mapping and subsequent topographic imaging. Suitable reflections had to be near the vertical axis as the diffractometer φ (perpendicular to the direct beam) and χ (parallel to the direct beam) axes were limited to about ±5.0° rotation each. Once a suitable reflection was chosen it was brought into the vertical plane of diffraction with the help of an off-line image-plate detector/reader. A rocking curve was then measured with the scintillation counter and fine adjustments were made to the goniometer circles to properly center the reflection in the detector aperture. The analyzer crystal was put in place and a reciprocal-space map was recorded by successive measurements at different sample and analyzer angular positions. During the data-collection process the total X-ray exposure time of the crystal varied, as several experiments are needed to locate and align desired reflections. Even so, we have seen no evidence of radiation damage in the specimens. Structural data collected on virgin samples and on samples subjected to our measurements showed no discernable difference. This is perhaps not too surprising given the narrow spectral and angular width of the beam with a commensurate reduction in intensity over a typical focused-beam structural data-collection experiment. Finally, a topograph was recorded with the sample in the maximum diffracting position derived from the reciprocal-space map and the film upstream of the analyzer.

Owing to time constraints and the technical limitations of the diffractometer it was not possible to index the crystals online, so different reflections at approximately the same resolution were examined in each case and indexed afterwards. Table 1 lists the crystals and reflections studied. Prior to reciprocal-space/topography studies, microgravity crystal μg 1 had a complete oscillation data set recorded on beamline X25 using a large MAR image plate. A complete data set was also recorded from a ground-control crystal on the same beamline in order to establish resolution limits. Similarly, data sets were collected from one microgravity and one ground-control crystal in the laboratory using a Rigaku RU-200 rotating-anode source with graphite-monochromated Mo Kα radiation and an R-AXIS IIC area detector, from which a detailed comparison of the protein and bound-solvent structure has been given (Dong *et al.*, 1999).

Table 1
Shown are the reflection chosen, the sample size, the $q_{\text{perpendicular}}$ and q_{parallel} at the full-width at half-maximum (FWHM) and at the width determined at 5% of the peak intensity (5%W) and the mosaicity resulting from the reciprocal-space analysis.

Crystal	h	k	l	Sample size (mm)	FWHM		5%W		η
					$q_{\text{perpendicular}}$ $(\times 10^{-4})$	q_{parallel} $(\times 10^{-4})$	$q_{\text{perpendicular}}$ $(\times 10^{-3})$	q_{parallel} $(\times 10^{-4})$	$(\times 10^{-3}\,°)$
Earth 1†	12	2	8	0.79 × 0.65 × 0.47	1.0		1.4	5.8	3.7
				0.79 × 0.65 × 0.47	1.7	1.1	1.2	5.2	2.1
Earth 2	18	2	0	0.37 × 0.33 × 0.30	2.7	0.64	0.54	7.4	7.2
Earth 3	17	10	4	0.51 × 0.45 × 0.26	2.2	2.0	1.1	5.8	6.4
Average									6.8
μg 1†	22	9	0	0.70 × 0.65 × 0.25	6.5	0.91	1.2	7.7	17.4
μg 2a‡	17	10	4	0.71 × 0.70 × 0.38	1.7	1.1	0.34	4.1	4.6
μg 2b‡	13	1	8	0.71 × 0.70 × 0.38	1.0	0.92	0.23	5.0	1.7
μg 3	4	2	8	0.25 × 0.25 × 0.23	2.6	2.1	0.74	7.3	7.2
μg 4	15	9	4	0.63 × 0.62 × 0.28	1.9	1.1	0.30	3.9	4.8
μg 5	13	7	5	0.68 × 0.65 × 0.43	1.9	2.1	0.73	9.6	4.8
Average									4.6

† $q_{\text{perpendicular}}$ and q_{parallel} values obtained for Earth 1, for which a split peak was observed in the reciprocal space, and crystal μg 1, which had a complete structural data set collected from it prior to the reciprocal-space mapping, were not considered in the calculation of average values. ‡ Crystal μg 2 was studied with two different reflections approximately 66° apart.

3.3. Purity analysis of the samples

The Sigma lysozyme preparations used in this study were analyzed using SDS–PAGE. This technique separates macromolecules according to molecular weight. In each case, the commercial preparations were supplied as lyophilized powder. S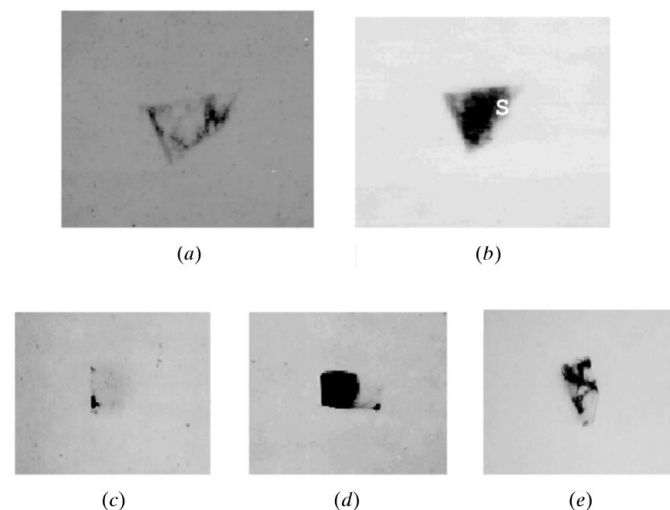tock solutions for analysis were prepared by dissolving each preparation in distilled water. The analysis was conducted using Phastgel gradient 8–25% gels with 10 000 ng sample loadings per lane on a Pharmacia PhastSystem (Pharmacia LKB Biotechnology, Piscataway, NJ). The heavily overloaded samples were used in order to detect macromolecule impurities. The gels were stained with both Coomassie blue stain (detection limit 20–30 ng per band) and the more sensitive enhanced silver stain (detection limit 0.3–0.5 ng per band; Amersham Pharmacia Biotech, Piscataway, NJ).

The stock lysozyme solutions used in this study varied in purity. That used for the LMS mission was found to contain impurity proteins of molecular weight 28 and 45 kDa and a very faint indication of an impurity at 80 kDa. These molecular weights are indicative of protein impurities often found in commercial lysozyme preparations and represent a lysozyme dimer (28 kDa), ovalbumin (45 kDa) and conalbumin (80 kDa) (Back, 1984; Lorber et al., 1993; Thomas et al., 1996; Judge et al., 1998). The sample used for the IML-2 mission was found to contain only the impurity at 28 kDa, with no trace of the higher molecular-weight impurities found in the LMS sample. Estimated lysozyme sample purity from the Coomassie blue stained gels were 99.2% for the IML-2 mission and 97.6% for the LMS mission. Both samples contained similar quantities of the lysozyme dimer (0.8%). A photograph of the silver-stained gel showing the impurities present in each sample has been submitted as supplementary material (Supplementary Fig. 1).[1]

After X-ray analysis, both the microgravity and ground-control crystals from the LMS mission were examined by SDS–PAGE analysis in order to determine crystal purity. The crystals were supplied in their capillaries, usually surrounded by a small amount of crystallization solution. A saturated solution produced from purified lysozyme (Forsythe et al., 1994) was used as a wash solution. For each crystal, the capillary was cut and the crystal removed by allowing wash solution to travel up the capillary and envelope the crystal, which was then pushed out of the capillary using a smaller diameter capillary tip. The crystal and some wash solution was pushed out on to a depression microscope slide and the crystal was then removed from the wash liquid. When all of the crystals had been collected, they were dissolved in 5 µl of water. The microgravity and ground-control grown samples

(a)　　　　　(b)

(c)　　　(d)　　　(e)

Figure 6
Monochromatic X-ray topographs of three lysozyme crystals grown on the IML-2 mission. Reflections were chosen to be in the 4.0–3.0 Å resolution shell. Magnification is 10×. Shown in (a) and (b) are two different reflections from a crystal grown in the laboratory as a control. Several structures can be observed: in (b) parallel lines may be a consequence of growth striations. (c) and (d) show topographs of two different reflections of a crystal grown in microgravity conditions. Shown in (e) is the topograph of another microgravity-grown crystal. Although crystals grown under microgravity conditions usually present few contrast structures, showing large regions of uniform contrast, few crystals have presented a rich contrast structure such as observed in (e). At present, we do not have a clear explanation as to why these exceptions occur.

[1] Supplementary materials are available from the IUCr electronic archive (Reference: ad0105). Services for accessing these data are described at the back of the journal.

were then run on an SDS–PAGE gel and stained with enhanced silver stain. This stain was used to enhance the sensitivity of the analysis in order to observe which impurities were present in the crystals, but did not permit quantitation.

4. Results

The topographs for some crystals grown during the IML2 mission are shown in Fig. 6. Each topograph corresponds to a different crystal and reflection. It was not possible for this study to index the different reflections, but each was chosen to be in the 3.5–3.0 Å resolution shell. For the LMS mission only the eight crystals mentioned above were studied, owing to restrictions on beam-time availability. From the five crystals grown in microgravity it was not possible to obtain an X-ray diffraction topograph for μg 3, owing to the weak diffraction presented by this crystal. The topographs and the reciprocal-space maps for the crystals are shown in Fig. 7. The corresponding (hkl) indices, the instrument-deconvoluted mosaicity values determined from rocking-curve measurements and their $q_{parallel}$ and $q_{perpendicular}$ values are shown in Table 1. Earth 1 and μg 1 are somewhat uncharacteristic samples: the former presents a split peak for the reflection studied which could not be observed on the diffraction pattern taken to survey the reflections, while the latter was submitted to a full oscillation data collection before the RSM measurements, which probably presented some deterioration owing to radiation damage.

As seen in Figs. 6 and 7, the topographs of ground-control grown crystals present more contrast structure, while topographs from crystals grown in microgravity conditions usually present one to three quite large regions with uniform contrast. Two exceptions are the topographs shown in Figs. 6(e) and 7(b). Fig. 6(e) shows the topograph from a microgravity-grown crystal (mission IML2) which presents a similar contrast structure to most ground-control crystals. The topograph shown in Fig. 7(b) is from crystal Earth 2, grown in the laboratory, and shows a rather uniform contrast quite unusual for crystals grown on the ground. Several features can be seen in both Figs. 6 and 7. One of them presents quite clearly (Fig. 7a) a broad bent line, labelled A in the figure. Region A_1 of this line shows a stronger contrast on the convex side (outer radius), while region A_2 presents a slightly stronger contrast on the concave side (inner radius) of the line. This feature, A, has been observed both on ground- and microgravity-grown crystals despite being less strong and sometimes having inverted contrast (inner radius stronger than outer radius) or no difference in contrast at all between any sides of the radius. To better visualize this feature, it was necessary to manipulate the images by inverting the contrast of the image (Image Magick version 4.2.9). Two of these processed images are shown in Fig. 8 and feature A is pointed out on them. It also seems that close to this feature there is either a circular feature directly connected to feature A (Fig. 8b) or an interruption similar to Fig. 8(a). Another feature commonly observed in topographs from ground-grown crystals are lines which are parallel to each other over a region or over the whole crystal,

labelled S in Fig. 6(b). For some samples, irrespective of their origin (ground- or microgravity-grown crystals), dark lines of variable length can be seen in some regions in the topograph. These lines are quite difficult to observe and even more difficult to reproduce clearly in a figure. It is not clear if they are of the same nature as the lines S in Fig. 6(b) or if they are an indication of a feature such as A in Fig. 7(a) or if they are of a completely different nature altogether.

We found that reciprocal-space maps and rocking-curve measurements allow a more quantitative comparison between the samples. Shown in Table 1 are the 'q' values determined at the FWHM (full-width at half-maximum) and at 5%W (width at 5% maximum intensity) as well as the average values found for $q_{parallel}$ and $q_{perpendicular}$. For the ground-control crystals, only two samples were taken into account. Because it presented a double peak, Earth 1 was not considered for the average calculation. The same was true for sample μg 1, which was submitted to oscillation data collection prior to topography/reciprocal-space mapping measurements. The reciprocal-space maps show clearly that $q_{parallel}$ from ground-control and microgravity crystals is essentially equal, while $q_{perpendicular}$ is slightly larger for ground-control crystals. This difference is even stronger when $q_{perpendicular}$ values at 5%W are considered. Larger values of $q_{perpendicular}$ can be associated with a larger amount of structures in the X-ray diffraction topography images. Therefore, for sample Earth 1 the $q_{perpendicular}$ values are 1.4 and 1.2×10^{-3}, the largest values found. These are also the topographs that present the most contrast structure and long tails in the $q_{perpendicular}$ direction. It is possible to determine a relation between the $q_{perpendicular}$ values at 5%W in Table 1 and the corresponding topographic images. Images which present more features and structure show higher $q_{perpendicular}$ values in reciprocal space. Excess diffuse scattering near Bragg peaks is expected for samples with large defect concentrations.

Oscillation data were collected on an LMS ground-control crystal ($0.7 \times 0.45 \times 0.4$ mm) and an LMS microgravity crystal ($0.7 \times 0.65 \times 0.3$ mm) on the NSLS X25 beamline using a 0.2 mm collimator and were processed using the *HKL* suite (Otwinowski & Minor, 1997). The microgravity crystal diffracted to 1.63 Å compared with 2.0 Å for the ground-control crystal, based on R_{merge} crossing 20%, with closely similar illuminated crystal volumes and under identical experimental conditions. The microgravity crystal yielded 59 processable images, whereas the ground control yielded 26 (see supplementary data).

For the LMS mission, analysis of the microgravity and ground-control crystals revealed that both samples contain the 28 kDa dimer (Back, 1984; Thomas *et al.*, 1996). In ground-based experiments this impurity is commonly found in lysozyme crystals (Skouri *et al.*, 1995; Thomas *et al.*, 1998) while the higher molecular-weight structurally different impurities were not present and were presumably excluded during the crystallization, both on the ground (Judge *et al.*, 1998) and in microgravity (Carter *et al.*, 1999). Given that silver stain was used for this analysis, it was not possible to quantitate the amount of the dimer impurity present in each crystal sample.

A photograph of the silver-stained gel showing the impurities present in each crystal sample has been submitted as supplementary material (Supplementary Fig. 2).

5. Discussion

Theoretical and experimental studies have suggested that microgravity could act as a purification mechanism during growth. In particular, Carter *et al.* (1999) noted that quantities of a naturally occurring dimer of lysozyme (Back, 1984; Thomas *et al.*, 1996) are reduced in microgravity compared with ground-control crystals and claimed that the structural data obtained from microgravity crystals was better than that from ground-control samples. Although very limited details are available on the actual data acquisition, it appears that they used quite different detector systems and data-collection strategies for the two cases (microgravity and ground control). Thus, although their conclusions regarding improved resolution limits are clear, their observation of improved B factors for the microgravity case is greatly weakened by this. Our structural data largely supports this observation in that we observe modest improvement in resolution limits for microgravity samples.

In our triple-axis measurements we observe almost identical $q_{parallel}$ for the two populations. This implies (i) no significant lattice-parameter inhomogeneity differences between the two populations and (ii) any domain-size effects are below our resolution limit (*i.e.* the correlation lengths are larger than roughly 3 μm). This suggests that microgravity has little or no effect on either of these properties within the capabilities of our measurement. In order to produce measurable strain effects, the material must have sufficient mechanical strength to support the strains necessary for its production. Lysozyme and other proteins are extremely fragile owing to their high solvent content and few molecular contacts. It seems plausible that the dominant response to local strains is plastic flow rather than elastic deformation; *i.e.* the lattice simply fragments to produce smaller unstrained segments.

The decreased values of $q_{perpendicular}$ for the microgravity samples indicate a better alignment of the mosaic blocks in that case. To gain more insight into this result we can refer to the topographic images. In general, samples showing a low $q_{perpendicular}$ display rather large homogeneous diffracting regions, whereas those showing higher values produce fragmented images with no clear correlation between the crystal regions diffracting at any particular angular setting. If the microgravity environment causes reduced impurity inclusions
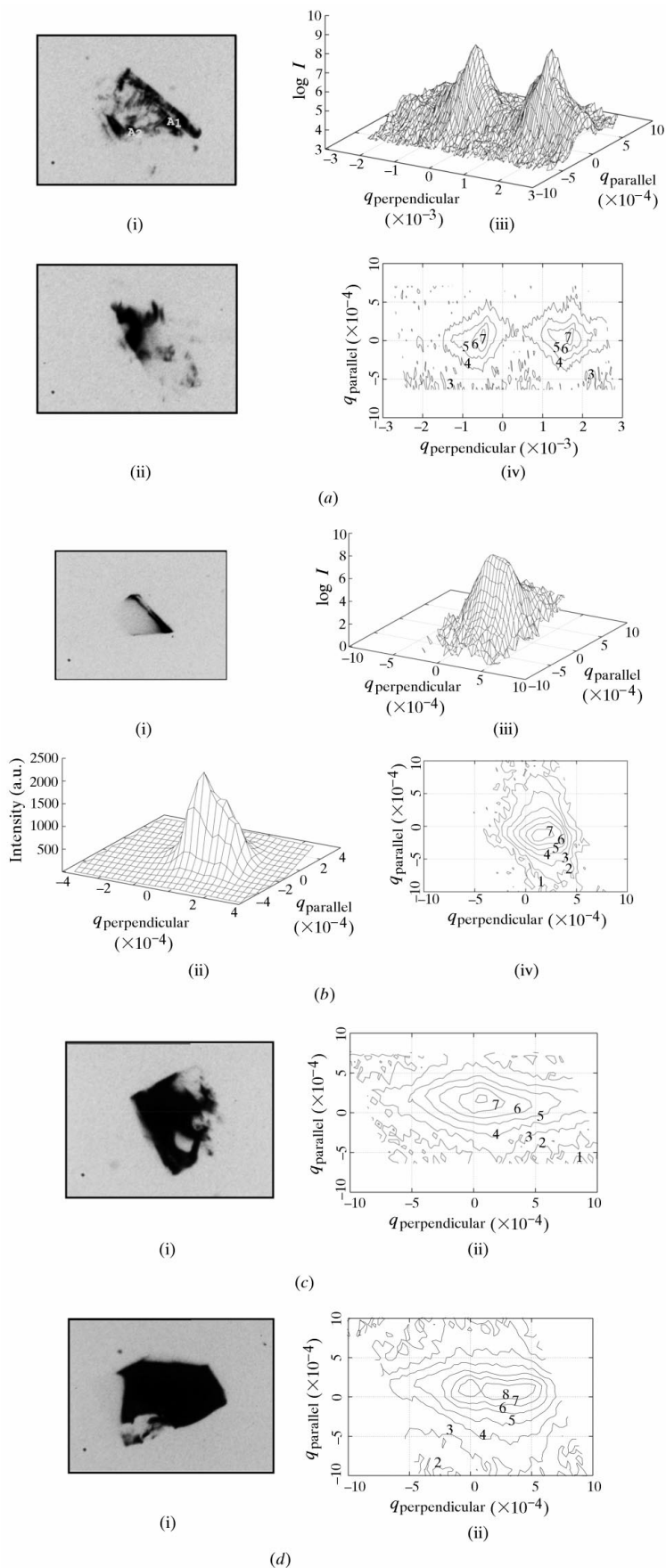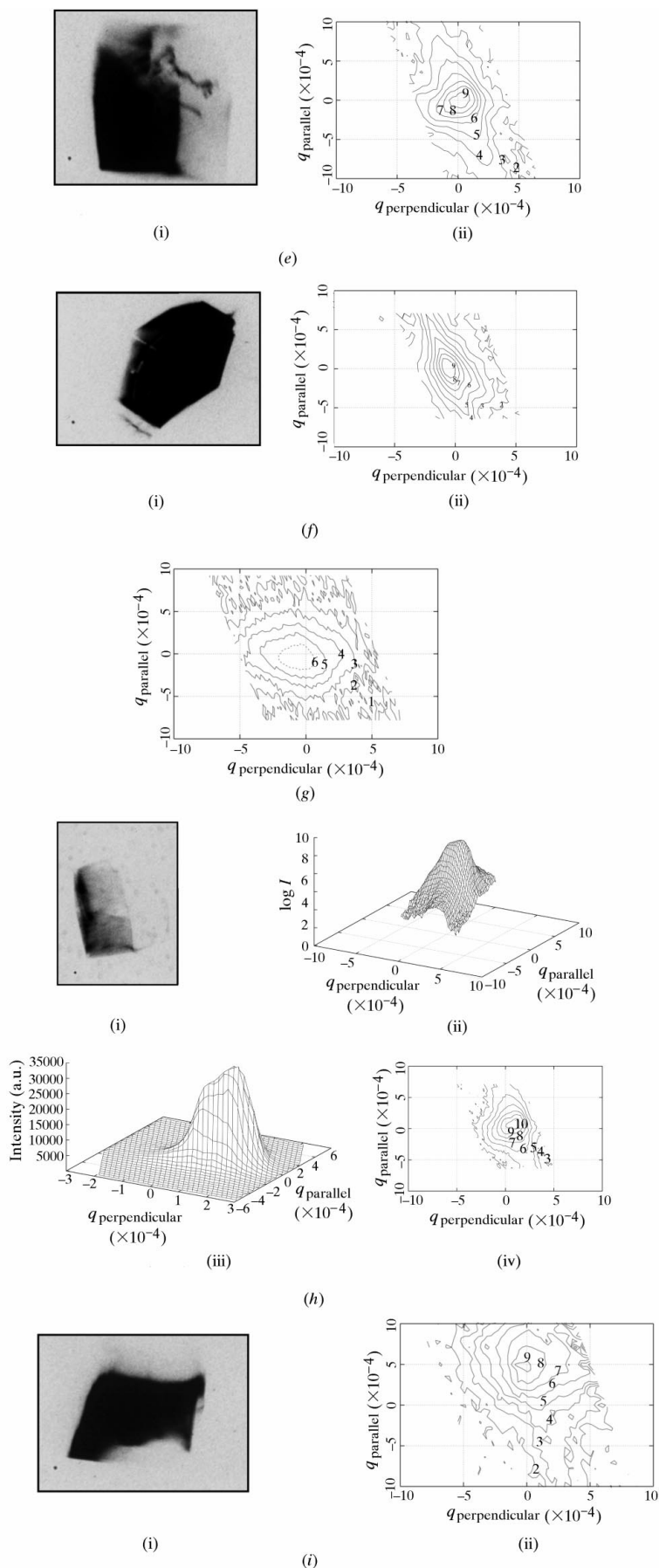

Figure 7

(i)   (ii)

(e)

(i)   (ii)

(f)

(g)

(i)   (ii)

(iii)   (iv)

(h)

(i)   (ii)

(i)

during growth, then it is possible that fewer lattice-disruptive events would occur, *i.e.* larger coherent regions would result, potentially with a lower mosaic spread. A reduction of mosaicity increases the peak height of the reflection whilst maintaining the integrated area in the kinematical limit (Snell *et al.*, 1995; Ng *et al.*, 1997). Ng *et al.* (1997) demonstrate the beneficial effect on the structural data from such decreased mosaicity.

The two samples measured at the synchrotron were measured under closely identical exposure conditions and utilizing similar illuminated volumes. The microgravity sample diffracted to 1.63 Å and the ground control to 2.0 Å. Even though this single data point does not by itself allow a conclusion, it is consistent with the results presented by Vaney *et al.* (1996). They observed that a microgravity sample (0.7 × 0.5 × 0.5 mm) produced similar data to a ground crystal (1.1 × 1.2 × 0.6 mm). This was for the same exposure time per image, but half the exposure time per degree of oscillation in the

Figure 7 (continued)
Shown is a summary of the X-ray topographic and reciprocal-space map studies for crystals grown during the LSM mission. Several views of the RSMs are shown for both samples Earth 2 and μg 4 because both present a rather uniform contrast in the topographs taken at the RSM intensity maxima. This is quite unusual for laboratory-grown crystals. A comparison of the RSM for both these samples, however, leads to differences of up to 70% in '*q*' values and, as seen in the figures, much larger in the case of Earth 2. With the exception of sample μg 1, which has been submitted to oscillation data collection prior to the RSM studies, microgravity-grown crystals present a slightly smaller spread in $q_{\mathrm{perpendicular}}$ than their counterparts grown on the ground. All topographs shown here have been recorded from film with the help of a metallographic microscope and have been enlarged 250×. (*a*) Earth 1, (i) and (ii) monochromatic X-ray topographs at the two intensity maxima shown in (iii); $q_{\mathrm{perpendicular}} = 1.696 \times 10^{-3}$ (i), $q_{\mathrm{perpendicular}} = -0.507 \times 10^{-3}$ (ii). (iii) RSM of the reflection listed in Table 1; the relative position of the topographs are indicated. (iv) contour diagram of the RSM shown in (iii) on a logarithmic scale. (*b*) Earth 2, (i) monochromatic X-ray topograph, (ii) and (iii) RSM showing $q_{\mathrm{perpendicular}}$ and q_{parallel}, (iv) contour diagram of the RSM shown in (ii) on a logarithmic scale. (*c*) Earth 3, (i) monochromatic X-ray topograph, (ii) contour diagram of the RSM on a logarithmic scale. (*d*) μg 1, (i) monochromatic X-ray topograph, (ii) contour diagram of the RSM on a logarithmic scale. (*e*) μg 2, (i) monochromatic X-ray topograph, (ii) contour diagram of the RSM on a logarithmic scale. μg 2a in Table 1. (*f*) μg 2, (i) monochromatic X-ray topograph, (ii) contour diagram of the RSM on a logarithmic scale. μg 2b in Table 1. (*g*) μg 3, contour diagram of the RSM on a logarithmic scale. (*h*) μg 4, (i) monochromatic X-ray topograph, (ii) and (iii) RSM showing $q_{\mathrm{perpendicular}}$ and q_{parallel}, (iv) contour diagram of the RSM shown in (ii) on a logarithmic scale. (*i*) (i) μg 5, monochromatic X-ray topograph, (ii) contour diagram of the RSM on a logarithmic scale.

microgravity case. Obviously, their microgravity crystal displayed a higher diffracting power given the difference in diffracting volume and it is unfortunate that the samples used were of such dissimilar volumes in their experiment. The Vaney *et al.* (1996) study used different biochemical conditions: 1.25 *M* NaCl and 1.65 *M* NaCl for microgravity and ground precipitant, respectively. For this study, we have kept the biochemical and physical conditions for our two sample populations essentially identical, excepting microgravity.

A study by Dobrianov *et al.* (1998) varying biochemical and physical conditions suggests a similar result in that mosaicity is increased but the lattice-parameter variation Δd is insensitive. This would imply that biochemical conditions have little effect on the lattice strains. Following the arguments given above, this is quite plausible.

In the case of μg 1, where a complete structural data set was collected prior to our RSM measurements, the crystal has a markedly increased $q_{perpendicular}$ compared with all the other microgravity crystals we studied, whilst $q_{parallel}$ remains similar. It is conceivable but unlikely that this is a coincidence

and that this sample was bad even before the data set was collected. It is more likely that there was degradation caused by the radiation exposure of the oscillation data collection. The mechanisms of crystal degradation following irradiation are worthy of future study. Again, note that the effect is almost entirely an increase in $q_{perpendicular}$.

6. Conclusions

Crystals from the LMS mission were examined in this study for the first time using triple-axis diffractometry and X-ray topography. Some samples from the IML-2 mission were studied using topography alone. The diffractometry results indicate that the different environments (ground and microgravity) do not (within the resolution of our instrument) affect the average lattice homogeneity, as would be evidenced by differing $q_{parallel}$. We do observe significant differences (about a factor of two) in $q_{perpendicular}$ for the two populations. The topographic images recorded suggest that the microgravity crystals show rather large contiguous volumes of crystal diffracting at a particular angle, whereas the ground crystals often showed many smaller separate volume elements contributing to the intensity. Using these observations, we postulate that the main deformation mode is a fragmentation of the crystal, possibly arising from different impurity inclusion rates in the two environments. The weakness of the molecular bonding in these crystals favors plastic flow, in the sense of lattice fragmentation, over elastic distortions to accommodate these impurities.

In Snell *et al.* (1995), mosaicity measurements were reported for two microgravity missions of differing durations. The shorter mission (Spacehab-1) yielded the lowest mosaicity values ever observed for protein crystals, interpreted as a crystal essentially comprising a single perfect block. The longer mission (IML-2) crystals, from which the presently studied samples were taken, showed larger rocking widths, although they were still significantly better than the respective ground-control crystals. This may be a consequence of the smaller crystal volume produced by the shorter growth period in the Spacehab experiment, since it is plausible that smaller crystals would contain fewer defects and hence have a lower $q_{perpendicular}$. This idea could be at the root of the commonly held view that in general smaller crystals are often 'better' than larger ones.

In future RSM experiments, it will be necessary to develop an instrument with much better $q_{parallel}$ resolution than our instrument if any strain or correlation-length studies are to be useful. In our instrument we could only resolve correlation lengths below 3 µm, whereas it is clear that the samples are better than that. The topographic images show regions of order 100 µm diffracting at the same time in the ground-control samples and up to the size of the crystal (0.5 mm) for the microgravity ones. Of course, this does not give a correlation length, but does give an upper limit to its possible value. On the other hand, our instrument appears to be quite adequate for $q_{perpendicular}$ measurements, at least for the current state of lysozyme crystal growth.
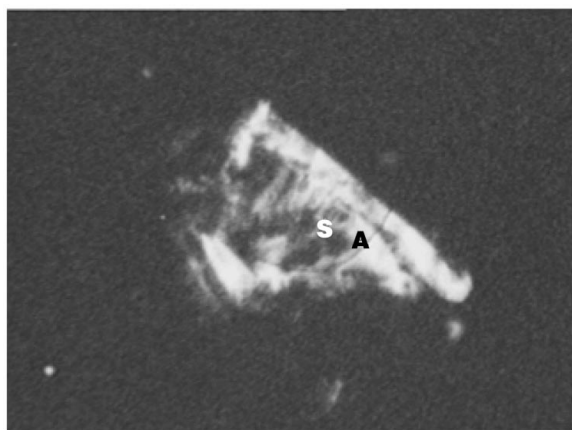
(*a*)
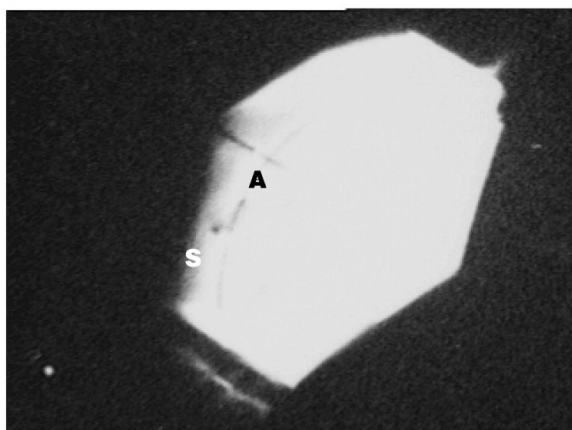
(*b*)

Figure 8
Reversed contrast X-ray topograph (Image Magick version 4.2.9) for samples (*a*) Earth 1 and (*b*) μg 2b showing the contrast characteristic of line A in Figs. 7(*a*) and 7(*f*). Lines S can also be seen in this figure. For further discussion refer to text.

Finally, it is clear that the variability between individual samples grown in any environment is quite large; to achieve any further conclusions many more samples must be examined and these samples must be grown as far as possible under identical conditions. It seems clear that the effect of microgravity is rather subtle and failure to compare like with like will only hinder understanding.

References

Alexander, L. E. & Smith, G. S. (1962). *Acta Cryst.* **15**, 983–1004.

Back, J. F. (1984). *Biochim. Biophys. Acta*, **799**, 319–321.

Baird, J. K., Meehan, E. J Jr, Xidis, A. L. & Howard, S. B. (1986). *J. Cryst. Growth*, **76**, 694–700.

Binnig, G., Quate, C. F. & Gerber, Ch. (1986). *Phys. Rev. Lett.* **56**, 930–933.

Boggon, T. J., Chayen, N. E., Snell, E. H., Dong, J., Lautenschlager, P., Potthast, L., Siddons, D. P., Stojanoff, V., Gordon, E., Thompson, A. W., Zagalsky, P. F., Bi, R.-C. & Helliwell, J. R. (1998). *Philos. Trans. R. Soc. London Ser. A*, **356**, 1045–1061.

Bosch, R., Lautenschlager, P., Potthast, L. & Stapelmann, J. (1992). *J. Cryst. Growth*, **122**, 310–316.

Bragg, L. & Nye, J. F. (1947). *Proc. R. Soc. London*, **190**, 474–481.

Brockhouse, B. N. (1955). *Phys. Rev.* **100**, 601–603.

Carter, D. C., Lim, K., Wright, B. S., Twigg, P. D., Miller, T. Y., Chapman, J., Keeling, K., Ruble, J., Vekilov, P. G., Thomas, B. R., Rosenberger, F. & Chernov, A. A. (1999). *J. Cryst. Growth*, **196**, 623–637.

Chayen, N. E., Snell, E. H., Helliwell, J. R. & Zagalsky, P. F. (1997). *J. Cryst. Growth*, **171**, 219–225.

Colapietro, M., Cappuccio, G., Marciante, C., Pifferi, A., Spagna, R. & Helliwell, J. R. (1992). *J. Appl. Cryst.* **25**, 192–194.

Darwin, C. G. (1922). *Philos. Mag.* **43**, 800–829.

DeLucas, L. J., Long, M. M., Rosenblaum, W. M., Bray, T. L., Smith, C., Carson, M., Narayana, S. V. L., Harrington, M. D., Carter, D. C., Clark, A. D. Jr, Nanni, R. G., Ding, J., Jacobo-Molina, A., Kamer, G., Hughes, S. H., Arnold, E., Einspahr, H. M., Clancy, L. L., Rao, G. S. J., Cook, P. F., Harris, B. G., Munson, S. H., Finzel, B. C., McPherson, A., Weber, P. C., Lewandowski, F. A., Nagabhushan, T. L., Trotta, P. P., Thompson, J. A., Richards, R. N., Bowersox, K. D., Meade, C. J., Baker, E. S., Bishop, S. P., Dunbar, B. J., Trinh, E., Prahl, J., Sacco, A. Jr & Bugg, C. E. (1994). *J. Cryst. Growth*, **135**, 183–195.

Dobrianov, I., Finkelstein, K. D., Lemay, S. G. & Thorne, R. E. (1998). *Acta Cryst.* D**54**, 922–937.

Dong, J., Boggon, T. J., Chayen, N. E., Raftery, J., Bi, R.-C. & Helliwell, J. R. (1999). *Acta Cryst.* D**55**, 745–752.

Fehribach, J. D. & Rosenberger, F. (1989). *J. Cryst. Growth*, **94**, 6–14.

Fewster, P. F. (1996). *X-ray and Neutron Dynamical Diffraction: Theory and Applications*, edited by A. Authier, S. Lagomarsino & B. W. Tanner, pp. 269–287. New York: Plenum Press.

Fewster, P. F. (1997). *Crit. Rev. Solid State Mater. Sci.* **22**, 69–110.

Fewster, P. F. & Andrew, N. L. (1993). *J. Appl. Phys.* **74**, 3121–3125.

Forsythe, E., Ewing, F. & Pusey, M. (1994). *Acta Cryst.* D**50**, 614–619.

Fourme, R., Ducruix, A., Riès-Kautt, M. & Capelle, B. (1995). *J. Synchrotron Rad.* **2**, 136–142.

Fourme, R., Ducruix, A., Riès-Kautt, M. & Capelle, B. (1999). *J. Cryst. Growth*, **196**, 535–545.

Grant, M. L. & Saville, D. A. (1991). *J. Cryst. Growth*, **108**, 8–18.

Greenhough, T. J. & Helliwell, J. R. (1982). *J. Appl. Cryst.* **15**, 338–351.

Helliwell, J. R. (1988). *J. Cryst. Growth*, **90**, 259–272.

Helliwell, J. R., Snell, E. H. & Weisgerber, S. (1996). *Proceedings of the 1995 Berlin Microgravity Conference*, edited by L. Ratke, H. Walter & B. Feuerbache, pp. 155–170. Berlin: Springer–Verlag.

Hilgenfeld, R., Liesum, A. & Storm, R. (1992). *J. Cryst. Growth*, **122**, 330–336.

Holý, V. & Mikulík, P. (1996). *X-ray and Neutron Dynamical Diffraction: Theory and Applications*, edited by A. Authier, S. Lagomarsino & B. K. Tanner, pp. 259–268. New York: Plenum Press.

Judge, R. A., Forsythe, E. L. & Pusey, M. L. (1998). *Biotechnol. Bioeng.* **59**, 776–785.

Kato, N. (1980). *Acta Cryst.* A**36**, 763.

Kuznetsov, Yu. G., Malkin, A. J., Glantz, W. & McPherson, A. (1996). *J. Cryst. Growth*, **168**, 63–73.

Lang, A. R. (1957). *Acta Metall.* **5**, 358–364.

Lin, H., Rosenberger, F., Alexander, J .I. D. & Nadarajah, A. (1995). *J. Cryst. Growth*, **151**, 153–162.

Long, M. M., DeLucas, L. J., Smith, C., Carson, M., Moore, K., Harrington, M. D., Pillion, D. J., Bishop, S. P., Rosenblum, W. M., Naumann, R. J., Chait, A., Prahl, J. & Bugg, C. E. (1994). *Int. J. Microgravity Res. Appl.* **7**, 196–202.

Lorber, B., Skouri, M., Munch, J. P., Giege, R. (1993). *J. Cryst. Growth*, **128**, 1203–1211.

McPherson, A. (1993). *J. Phys. D*, **26**, B104–B112.

McPherson, A., Malkin, A. J., Kuznetsov, Y. G., Koszelak, S., Wells, M., Jenkins, G., Howard, J. & Lawson, G. (1999). *J. Cryst. Growth*, **196**, 572–586.

Marangoni, C. G. M. (1871). *Ann. Phys. Chem. (Poggendorf)*, **143**, 337–345.

Molenkamp, T. (1998). *Marangoni Convection, Mass Transfer and Microgravity*. PhD thesis, Rijksuniversiteit Groningen, The Netherlands.

Monaco, L. A. & Rosenberger, F. (1993). *J. Cryst. Growth*, **129**, 465–484.

Nave, C. (1998). *Acta Cryst.* D**54**, 848–853.

Nerad, B. A. & Shlichta, P. J. (1986). *J. Cryst. Growth*, **75**, 591–608.

Ng, J. D., Lorber, B., Giegé, R., Koszelak, S., Day, J., Greenwood, A. & McPherson, A. (1997). *Acta Cryst.* D**53**, 724–733.

Otalora, F., Garcia-Ruiz, J. M., Gavira, J. A & Capelle, B. (1999). *J. Cryst. Growth*, **196**, 546–558.

Otwinowski, Z. & Minor, W. (1997). *Methods Enzymol.* **276**, 307–326.

Pusey, M. L., Snyder, R. S. & Naumann, R. J. (1986). *J. Biol. Chem.* **261**, 6524–6529.

Pusey, M., Witherow, W. & Naumann, R. (1988). *J. Cryst. Growth*, **90**, 105–111.

Savino, R. & Monti, R. (1996). *J. Cryst. Growth.* **165**, 308–318.

Shaikevitch, A. & Kam, Z. (1981). *Acta Cryst.* A**37**, 871–875.

Skouri, M., Lorber, B., Giegé, R., Munch, J. P. & Candau, J. S. (1995). *J. Cryst. Growth*, **152**, 209–220.

Snell, E. H. (1998). *Proceedings of the Spacebound 1997 Conference*, pp. 306–315. Canadian Space Agency.

Snell, E. H., Boggon, T. J., Helliwell, J. R., Moskowitz, M. E. & Nadarajah, A. (1997). *Acta Cryst.* D**53**, 747–755.

Snell, E. H., Helliwell, J. R., Boggon, T. J., Lautenschlager, P. & Potthast, L. (1996). *Acta Cryst.* D**52**, 529–533.

Snell, E. H., Weisgerber, S., Helliwell, J. R., Weckert, E., Hölzer, K. & Schroer, K. (1995). *Acta Cryst.* D**51**, 1099–1102.

Snyder, R. S., Fhurmann, K. & Walter, H. U. (1991). *J. Cryst. Growth*, **110**, 333–338.

Stojanoff, V. & Siddons, D. P. (1996). *Acta Cryst.* A**52**, 498–499.

Stojanoff, V., Siddons, D. P., Monaco, L., Vekilov, P. & Rosenberger, F. (1997). *Acta Cryst.* D**53**, 588–595.

Stojanoff, V., Siddons, D. P., Snell, E. H. & Helliwell, J. R. (1996). *Synchrotron Radiat. News*, **9**, 25–26.

Takagi, S. (1969). *Acta Cryst.* **15**, 1311.

Tanner, B. K. (1996). *X-ray and Neutron Dynamical Diffraction: Theory and Applications*, edited by A. Authier, S. Lagomarsino & B. K. Tanner, pp. 147–166. New York: Plenum Press.

Taupin, D. (1964). *Bull. Soc. Fr. Mineral. Cristallogr.* **57**, 469–511.

Teeter, M. M., Roe, M. S. & Heo, N. H. (1993). *J. Mol. Biol.* **230**, 292–311.

Thomas, B. R., Vekilov, P. G. & Rosenberger, F. (1996). *Acta Cryst.* D**52**, 776–784.

Thomas, B. R., Vekilov, P. G. & Rosenberger, F. (1998). *Acta Cryst.* D**54**, 226–236.

Vaney, M. C., Maignan, S., Riès-Kautt, M. & Ducriux, A. (1996). *Acta Cryst.* D**52**, 505–517.

Vekilov, P. G. & Rosenberger, F. (1996). *J. Cryst. Growth*, **158**, 540–551.

Wilcox, W. R. (1983). *J. Cryst. Growth*, **65**, 133–142.